

Article

2-Chloroalkoxy-Substituted Pentafluorinated Bistolanes as Novel Light-Emitting Liquid Crystals

Shigeyuki Yamada ^{1,*} , Kazuya Miyano ¹, Tomohiro Agou ² , Toshio Kubota ² and Tsutomu Konno ¹

¹ Faculty of Molecular Chemistry and Engineering, Kyoto Institute of Technology, Matsugasaki, Sakyo-ku, Kyoto 606-8585, Japan; kit.fusso.201601@gmail.com (K.M.); konno@kit.ac.jp (T.K.)

² Department of Quantum Beam Science, Graduate School of Science and Engineering, Ibaraki University, 4-12-1 Naka-narusawa, Hitachi, Ibaraki 316-8511, Japan; tomohiro.agou.mountain@vc.ibaraki.ac.jp (T.A.); toshio.kubota.organicchem@vc.ibaraki.ac.jp (T.K.)

* Correspondence: syamada@kit.ac.jp; Tel.: +81-75-724-7517

Received: 19 March 2019; Accepted: 3 April 2019; Published: 6 April 2019



Abstract: In this study, we designed and synthesized novel pentafluorinated bistolane derivatives with 2-chloropentyl or 2-chlorohexyl flexible units as novel light-emitting liquid crystals (LELCs). By measuring the phase-transition behaviors, all derivatives were found to display liquid-crystalline (LC) phases during both heating and cooling processes. Among the novel bistolanes, the *S*- and *R*-configured derivatives exhibited a chiral nematic (N*) phase with a typical Grandjean optical texture. Interestingly, the chiral derivatives also exhibited a blue phase with a typical platelet texture in a narrow temperature range (2–4 °C). Photophysical measurements revealed that the 2-chloroalkoxy-substituted pentafluorinated bistolanes exhibited intense photoluminescence (PL) both in solution and in crystalline phases. The PL characteristics, especially the maximum PL wavelength, were found to switch sensitively during the heating and cooling cycles depending on the molecular aggregates through the crystal (Cr) \rightleftharpoons N* phase transition. The 2-chloroalkoxy flexible units induced dynamic changes in the LC and PL properties, providing valuable insight into the potential of various LELCs as PL sensing materials.

Keywords: liquid crystal; photoluminescence; fluorine; bistolane structure; chirality

1. Introduction

Organic light-emitting (LE) materials have become widely used in our lives, for example, in biomedical imaging, optical probes, light-emitting diodes, and electroluminescent displays [1–5]. Most LE molecules have extended π -conjugations and emit intense luminescence in dilute solution, which is essential for the first two of the aforementioned applications [6,7]. It is known, however, that π -conjugated LE molecules cannot be applied in the last two applications because their luminescence smoothly quenches with the formation of molecular aggregates due to the aggregation-caused quenching effect [8,9]. Since Tang et al. discovered an intriguing luminescence phenomenon in which the luminescence intensity of the aggregated forms dramatically increases through restriction of intermolecular motion [10], significant efforts have been devoted to the development of organic LE molecules showing photoluminescence (PL) in condensed phases [11,12].

Recently, our group developed families of pentafluorinated tolane [13] and bistolane derivatives with alkoxy-type flexible chains (Figure 1a) [14,15] as promising LE materials and revealed that their PL can change depending on the electron-density distribution [16] or the molecular arrangement in the aggregated structure [13–15]. It was of great interest that the bistolane-type LE molecules showed not only PL, but also liquid-crystalline (LC) properties, namely light-emitting liquid crystals

(LELCs) [17–20], and the PL behaviors were found to change through the crystal (Cr) \rightleftharpoons LC thermal phase transition. In addition, we recently developed novel LELCs with V- or Y-shaped molecular geometry, which showed intriguing switching characteristics induced by thermal stimulus [21].

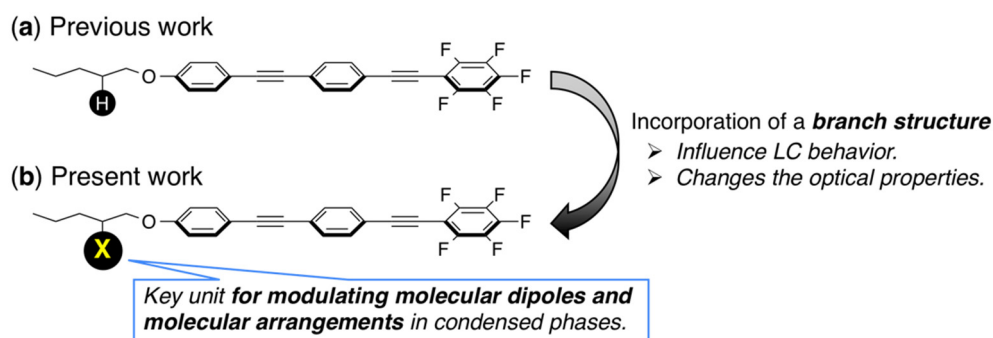


Figure 1. Structures studied in (a) a previous study and (b) the present work for the development of light-emitting liquid crystal (LELC) molecules. LC: liquid crystal.

We subsequently directed our attention toward novel pentafluorinated bistolane-type LELCs with branch structures in their flexible units because the electric or steric effect can induce dynamic changes of molecular dipoles and molecular arrangements in condensed phases (Figure 1B). Therefore, in this article, we describe the molecular design and synthesis of novel pentafluorinated bistolane-type LELCs carrying flexible units with the branch structure shown in Figure 1b and present detailed evaluations of their LC and PL properties. The PL characteristics of the present bistolane-type LELCs under heating and cooling processes are discussed as well.

2. Materials and Methods

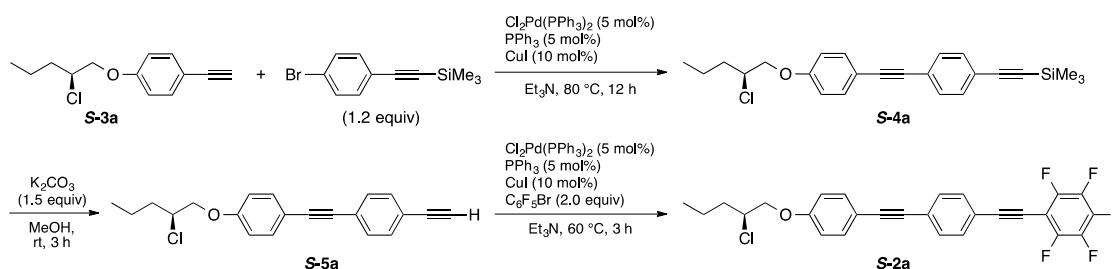
2.1. General

^1H and ^{13}C NMR spectra were recorded using a Bruker AVANCE III 400 NMR spectrometer (Rheinstetten, Germany) (^1H : 400 MHz and ^{13}C : 100 MHz) in chloroform-*d* (CDCl_3) solution, and the chemical shifts are reported in parts per million (ppm) using the residual proton in the NMR solvent. ^{19}F NMR (376 MHz) spectra were acquired using a Bruker AVANCE III 400 NMR spectrometer (Rheinstetten, Germany) in CDCl_3 solution with CFCl_3 ($\delta_{\text{F}} = 0$ ppm) as an internal standard. Infrared (IR) spectra were acquired from KBr pellets containing the samples using a JASCO FT/IR-4100 type A spectrometer (Tokyo, Japan); all spectra are reported in wavenumber (cm^{-1}). High-resolution mass spectroscopy (HRMS) was performed using a JEOL JMS-700MS spectrometer (Tokyo, Japan) via fast atom bombardment (FAB). All reactions were performed using dried glassware with a magnetic stir bar. All chemicals were of reagent grade, and they were purified in the usual manner prior to use when necessary. Column chromatography was conducted using silica gel (FUJIFILM Wako Pure Chemical Corporation, Wako-gel®60 N, 38–100 μm ; Osaka, Japan) and thin layer chromatography (TLC) was performed on silica gel TLC plates (Merck, Silica gel 60F₂₅₄; New Jersey, NJ, USA).

2.2. Materials

According to the synthetic procedure shown in Scheme 1, the pentafluorinated bistolanes with the branched flexible chain **2a** used in this study were prepared from 4-(2-chloropentyloxy)phenylacetylene (**3a**), which was accessible from commercially available norvaline [15]. The *S*- and *R*-configured **2a**, i.e., *S*-**2a** and *R*-**2a**, as well as a racemic mixture (*rac*-**2a**) were obtained in the same manner using the corresponding *S*-/*R*- or racemic norvaline. With commercially available *S*- or racemic norleucine, other analogues, e.g., *S*-**2b** and *rac*-**2b**, were obtained with the same synthetic sequence. Since the chemical properties of the chiral and racemic mixtures were the same, typical synthetic procedures and the spectral data only for *S*-configured *S*-**2a** and *S*-**2b** are reported below as selected examples. The

molecular structures of bistolane **2a** and **2b** were characterized via spectroscopic analyses, such as ^1H , ^{13}C , and ^{19}F NMR spectroscopy; infrared (IR) spectroscopy; and HRMS. The NMR spectra indicated that the products were sufficiently pure for the evaluation of their LC and PL properties.



Scheme 1. Typical synthetic procedure for (S)-2-chloropentyloxy-substituted pentafluorinated bistolanes **S-2a**.

2.3. Typical Procedure for the Preparation of *S-4a*

In a 50-mL two-necked, round-bottomed flask with a Teflon-coated stir bar and reflux condenser, 1-bromo-4-[2-(trimethylsilyl)ethyn-1-yl]benzene (1.8 g, 7.2 mmol), $\text{Cl}_2\text{Pd}(\text{PPh}_3)_2$ (0.21 g, 0.30 mmol), PPh_3 (80 mg, 0.30 mmol), CuI (0.12 g, 0.60 mmol), and Et_3N (10 mL) were placed. Then, a solution of (S)-2-chloropentyloxyphenylacetylene (**S-3a**, 1.4 g, 6.0 mmol) dissolved in Et_3N (30 mL) was added to the solution. The whole mixture was stirred at 80 °C for 12 h. The precipitate formed in the reaction mixture was separated by atmospheric filtration and the filtrate was poured into aqueous NH_4Cl solution (20 mL). The crude product was extracted using AcOEt (20 mL, three times) and washed with brine (20 mL, once). The organic layer was collected, dried over anhydrous Na_2SO_4 , filtered, and concentrated in vacuo using a rotary evaporator. The resultant crude product was purified via silica-gel column chromatography using hexane as the eluent to obtain the desired product (**S-4a**, 1.1 g, 2.7 mmol) in 45% yield, as a white solid.

2-[4-[2-(2-Chloropentyloxy)phenylethyn-1-yl]phenylethyn-1-yl]trimethylsilane (*S-4a*)

Yield: 45%; M.P.: 77–78 °C; ^1H NMR (CDCl_3): δ 0.25 (s, 9H), 0.97 (t, $J = 7.2$ Hz, 3H), 1.42–1.54 (m, 1H), 1.60–1.70 (m, 1H), 1.71–1.83 (m, 1H), 1.90–2.01 (m, 1H), 4.06–4.25 (m, 3H), 6.89 (d, $J = 8.8$ Hz, 2H), 7.43 (brs, 4H), 7.46 (d, $J = 8.8$ Hz, 2H); ^{13}C NMR (CDCl_3): δ -0.1, 13.5, 19.3, 36.8, 59.1, 71.8, 88.0, 91.1, 96.1, 104.7, 114.7, 115.7, 122.6, 123.6, 131.2, 131.9, 133.1, 158.4; IR ν 3041, 2959, 2897, 2340, 2214, 1568, 1405, 1249, 1104, 1041, 841 cm^{-1} ; HRMS (FAB+) m/z $[\text{M}]^+$ calcd for $\text{C}_{24}\text{H}_{27}\text{ClOSi}$: 394.1520; found: 394.1525.

2.4. Typical Procedure for the Preparation of *S-4b*

In a 50-mL two-necked, round-bottomed flask equipped with a Teflon-coated stir bar and reflux condenser, 1-bromo-4-[2-(trimethylsilyl)ethyn-1-yl]benzene (3.2 g, 13 mmol), $\text{Cl}_2\text{Pd}(\text{PPh}_3)_2$ (0.37 g, 0.53 mmol), PPh_3 (0.14 g, 0.53 mmol), CuI (0.42 g, 1.1 mmol), and Et_3N (10 mL) were placed. Then, a solution of (S)-2-chloropentyloxyphenylacetylene (**S-3b**, 2.5 g, 11 mmol) in Et_3N (30 mL) was added to the solution. Subsequently, the reaction mixture was stirred at 80 °C for 12 h. The precipitate formed in the reaction mixture was separated by atmospheric filtration and the filtrate was poured into aqueous NH_4Cl solution (20 mL). The crude product was extracted using AcOEt (20 mL, three times) and washed with brine (20 mL, once). The collected organic layer was dried over anhydrous Na_2SO_4 , filtered, and concentrated in vacuo using a rotary evaporator. The resultant crude product was purified via silica-gel column chromatography using hexane as the eluent to obtain the desired product (**S-4b**, 1.3 g, 3.1 mmol) in 28% yield, as a white solid.

2-[4-[2-(2-Chlorohexyloxy)phenylethyn-1-yl]phenylethyn-1-yl]trimethylsilane (S-4b)

Yield: 28%; M.P.: 81–82 °C; $^1\text{H NMR}$ (CDCl_3): δ 0.25 (s, 9H), 0.94 (t, $J = 7.6$ Hz, 3H), 1.28–1.51 (m, 3H), 1.56–1.66 (m, 1H), 1.71–1.84 (m, 1H), 1.94–2.03 (m, 1H), 4.06–4.21 (m, 3H), 6.89 (d, $J = 8.8$ Hz, 2H), 7.43 (brs, 4H), 7.46 (d, $J = 8.8$ Hz, 2H); $^{13}\text{C NMR}$ (CDCl_3): δ -0.1, 13.9, 22.2, 28.2, 34.4, 59.4, 71.7, 87.9, 91.2, 96.1, 104.7, 114.7, 115.7, 122.6, 123.6, 131.2, 131.8, 133.1, 158.4; IR ν 2958, 2862, 2213, 2157, 1515, 1465, 1249, 1175, 1045, 913, 846 cm^{-1} ; HRMS (FAB+) m/z [M] $^+$ calcd for $\text{C}_{25}\text{H}_{29}\text{ClOSi}$: 408.1676; found: 408.1671.

2.5. Typical Procedure for the Preparation of S-5a

In a 50-mL round-bottomed flask, freshly obtained **S-4a** (1.0 g, 2.6 mmol) and K_2CO_3 (0.6 g, 4.2 mmol) in MeOH (10 mL) were placed, and the solution was continuously stirred at room temperature for 3 h. The solvent, MeOH, was evaporated from the resultant mixture, followed by the addition of aqueous NH_4Cl solution (20 mL). The crude product was extracted using AcOEt (20 mL, three times) and washed with brine (20 mL, once). The collected organic layer was dried over anhydrous Na_2SO_4 , filtered, and concentrated under reduced pressure using a rotary evaporator. The resultant product was purified via silica-gel column chromatography (eluent: hexane) to obtain the desired product (**S-5a**, 0.85 g, 2.6 mmol) in a quantitative yield, as a white solid.

4-[2-(2-Chloropentyloxy)phenylethyn-1-yl]phenylacetylene (S-5a)

Yield: 100%; M.P.: 89–90 °C; $^1\text{H NMR}$ (CDCl_3): δ 0.98 (t, $J = 7.6$ Hz, 3H), 1.42–1.53 (m, 1H), 1.60–1.72 (m, 1H), 1.73–1.84 (m, 1H), 1.89–2.02 (m, 1H), 3.17 (s, 1H), 4.06–4.24 (m, 3H), 6.89 (d, $J = 8.8$ Hz, 2H), 7.45 (brs, 4H), 7.47 (d, $J = 8.8$ Hz, 2H); $^{13}\text{C NMR}$ (CDCl_3): δ 13.6, 19.4, 36.8, 59.1, 71.7, 78.8, 83.3, 87.8, 91.2, 114.7, 115.6, 121.5, 124.0, 131.3, 132.0, 133.2, 158.5; IR ν 2960, 2873, 2360, 2215, 1515, 1457, 1247, 1174, 1107, 978, 842 cm^{-1} ; HRMS (FAB+) m/z [M] $^+$ calcd for $\text{C}_{21}\text{H}_{19}\text{ClO}$: 322.1224; found: 322.1119.

2.6. Typical Procedure for the Preparation of S-5b

In a 50-mL round-bottomed flask, freshly obtained **S-4b** (0.50 g, 1.2 mmol) and K_2CO_3 (0.27 g, 1.9 mmol) in MeOH (10 mL) were placed, and the solution was continuously stirred at room temperature for 3 h. The solvent MeOH was evaporated, followed by the addition of aqueous NH_4Cl solution (20 mL). The crude product was extracted with AcOEt (20 mL, three times) and washed with brine (20 mL, once). The collected organic layer was dried over anhydrous Na_2SO_4 , filtered, and concentrated under reduced pressure using a rotary evaporator. The resultant product was purified via silica-gel column chromatography (eluent: hexane) to obtain the desired product (**S-5b**, 0.41 g, 1.2 mmol) in a quantitative yield, as a white solid.

4-[2-(2-Chlorohexyloxy)phenylethyn-1-yl]phenylacetylene (S-5b)

Yield: 100%; M.P.: 89–90 °C; $^1\text{H NMR}$ (CDCl_3): δ 0.94 (t, $J = 7.2$ Hz, 3H), 1.30–1.50 (m, 3H), 1.56–1.65 (m, 1H), 1.72–1.86 (m, 1H), 1.93–2.04 (m, 1H), 3.17 (s, 1H), 4.05–4.22 (m, 3H), 6.89 (d, $J = 8.8$ Hz, 2H), 7.45 (brs, 4H), 7.47 (d, $J = 8.8$ Hz, 2H); $^{13}\text{C NMR}$ (CDCl_3): δ 13.9, 22.1, 28.2, 34.4, 59.4, 71.7, 78.8, 83.3, 87.8, 91.2, 114.7, 115.6, 121.5, 124.0, 131.3, 132.0, 133.1, 158.4; IR ν 3040, 2958, 2863, 2359, 2215, 1606, 1458, 1248, 1174, 1072, 974, 839 cm^{-1} ; HRMS (FAB+) m/z [M] $^+$ calcd for $\text{C}_{22}\text{H}_{21}\text{ClO}$: 336.1281; found: 336.1290.

2.7. Typical Procedure for the Preparation of S-2a

In a 50-mL two-necked, round-bottomed flask equipped with a stir bar and reflux condenser, bromopentafluorobenzene (0.75 g, 3.0 mmol), $\text{Cl}_2\text{Pd}(\text{PPh}_3)_2$ (60 mg, 0.10 mmol), PPh_3 (80 mg, 0.13 mmol), and CuI (29 mg, 0.17 mmol) in Et_3N (10 mL) were placed. Then, a solution of **S-5a** (0.49 g, 1.5 mmol) in Et_3N (5.0 mL) was added to this mixture. The whole mixture was stirred at 60 °C for 3 h. The precipitate formed in the reaction mixture was separated by atmospheric filtration, and the filtrate

was poured into aqueous NH_4Cl solution (20 mL). The crude product was extracted using AcOEt (20 mL, three times) and washed with brine (20 mL, once). The collected organic layer was dried over anhydrous Na_2SO_4 , filtered, and concentrated in vacuo. The resultant product was purified via silica-gel column chromatography (eluent: hexane/AcOEt = 20/1) to obtain the desired product (**S-2a**, 0.25 g, 0.52 mmol) in 35% yield, as a white solid. This product was recrystallized from $\text{CH}_2\text{Cl}_2/\text{MeOH}$ (1/1) by slow evaporation of the solvent to obtain the title compound in crystal form.

1-[2-(2-Chloropentyloxy)phenylethyn-1-yl]-4-[2-(2,3,4,5,6-pentafluorophenyl)ethyn-1-yl]benzene (**S-2a**)

Yield: 35%; M.P.: 130 °C determined by a differential scanning calorimeter (DSC); ^1H NMR (CDCl_3): δ 0.98 (t, J = 7.2 Hz, 3H), 1.45–1.55 (m, 1H), 1.59–1.69 (m, 1H), 1.71–1.82 (m, 1H), 1.91–1.99 (m, 1H), 4.91–4.23 (m, 3H), 6.90 (d, J = 8.8 Hz, 2H), 7.48 (d, J = 8.8 Hz, 2H), 7.51 (d, J = 8.8 Hz, 2H), 7.55 (d, J = 8.8 Hz, 2H); ^{13}C NMR (CDCl_3): δ 13.5, 19.3, 36.8, 59.1, 71.8, 74.6 (q, J = 3.6 Hz), 87.8, 92.0, 100.2 (td, J = 19.1, 2.9 Hz), 101.2 (d, J = 2.9 Hz), 114.9, 115.6, 120.8, 124.9, 131.8, 133.2, 136.2–139.2 (dm, J = 250.3 Hz), 140.0–143.1 (dm, 256.6 Hz), 145.7–148.4 (dm, J = 251.8 Hz), 158.6; ^{19}F NMR: δ -136.42 (dd, J = 21.8, 6.8 Hz, 2F), -152.9 (t, J = 21.8 Hz, 1F), 162.21 (td, J = 21.8, 6.8 Hz, 2F); IR (KBr): ν 2931, 2865, 2364, 2204, 1525, 1497, 1287, 1178, 960, 837 cm^{-1} ; HRMS (FAB+) m/z [M] $^+$ calcd for $\text{C}_{27}\text{H}_{18}\text{ClF}_5\text{O}$: 488.0966; found: 488.0969.

2.8. Typical Procedure for the Preparation of **S-2b**

In a 50-mL two-necked, round-bottomed flask equipped with a stir bar and reflux condenser, bromopentafluorobenzene (0.54 g, 2.2 mmol), $\text{Cl}_2\text{Pd}(\text{PPh}_3)_2$ (38 mg, 0.055 mmol), PPh_3 (15 mg, 0.056 mmol), and CuI (0.023 mg, 0.12 mmol) in Et_3N (10 mL) were placed. A solution of **S-5b** (0.37 g, 1.1 mmol) dissolved in Et_3N (5.0 mL) was added to this solution. The whole mixture was stirred at 60 °C for 3 h. The precipitate formed in the reaction mixture was separated by atmospheric filtration, and the filtrate was poured into aqueous NH_4Cl solution (20 mL). The crude product was extracted using AcOEt (20 mL, three times) and washed with brine (20 mL, once). The collected organic layer was dried over anhydrous Na_2SO_4 , filtered, and concentrated in vacuo. The resultant product was purified via silica-gel column chromatography (eluent: hexane/AcOEt = 20/1) to obtain the desired product (**S-2b**, 0.27 g, 0.53 mmol) in 48% yield, as a white solid. This product was recrystallized from $\text{CH}_2\text{Cl}_2/\text{MeOH}$ (1/1) by slow evaporation of the solvent to obtain the title compound in crystal form.

1-[2-(2-Chlorohexyloxy)phenylethyn-1-yl]-4-[2-(2,3,4,5,6-bentafluorophenyl)ethyn-1-yl]benzene (**S-2b**)

Yield: 48%; M.P.: 130 °C determined by DSC; ^1H NMR (CDCl_3): δ 0.94 (t, J = 7.2 Hz, 3H), 1.31–1.51 (m, 2H), 1.59–1.64 (m, 1H), 1.73–1.83 (m, 1H), 1.94–2.05 (m, 1H), 4.07–4.23 (m, 3H), 6.90 (d, J = 8.8 Hz, 2H), 7.48 (d, J = 8.8 Hz, 2H), 7.51 (d, J = 8.4 Hz, 2H), 7.55 (d, J = 8.4 Hz, 2H); ^{13}C NMR (CDCl_3): δ 13.9, 22.2, 28.8, 34.5, 59.4, 71.8, 74.6 (d, J = 2.2 Hz), 87.8, 92.0, 100.2 (td, J = 20.4, 3.6 Hz), 101.2, 114.8, 115.6, 120.8, 124.9, 131.4, 131.8, 133.2, 136.3–139.3 (dm, J = 249.3 Hz), 139.8–143.3 (dm, J = 242.0 Hz), 145.7–148.8 (dm, J = 245.7 Hz), 158.6; ^{19}F NMR (CDCl_3): δ -136.42 (dd, J = 20.3, 6.8 Hz, 2F), -152.92 (t, J = 20.3 Hz, 1F), -162.21 (td, J = 20.3, 6.8 Hz, 2F); IR (KBr): ν 2940, 2875, 2365, 2204, 1569, 1497, 1286, 1219, 1178, 1080, 992, 838 cm^{-1} ; HRMS (FAB+) m/z [M] $^+$ calcd for $\text{C}_{28}\text{H}_{20}\text{ClF}_5\text{O}$: 502.1123; found: 502.1147.

2.9. X-ray Crystallography

Single crystals of 2-chloroalkoxy-substituted pentafluorinated bistolanes, e.g., **S-2a**, **R-2a**, and **S-2b**, were obtained through column chromatography purification followed by recrystallization ($\text{CH}_2\text{Cl}_2/\text{MeOH}$ = 1/1). The so-obtained single crystals were mounted on a glass fiber. X-ray diffraction patterns were recorded on a Rigaku XtaLabMini diffractometer or a Rigaku Saturn 724 diffractometer equipped with a VariMax Mo optic system (Tokyo, Japan) using $\text{CuK}\alpha$ radiation (λ = 1.54187 Å). The reflection data were integrated, scaled, and averaged using the CrysAlisPro (ver. 1.171.38.46, Rigaku Oxford Diffraction, 2015). Empirical absorption corrections were applied using the SCALE3 ABSPACK scaling algorithm (CrysAlisPro). The structures were solved by a

directed method (SHELXT-2014/5) and refined using a full-matrix least square method on F^2 for all reflections (SHELXL-2014/7) [22]. The crystallographic data were deposited into the Cambridge Crystallographic Data Centre (CCDC; Cambridge, UK) database (CCDC 1896325 for **S-2a**, 1896324 for **R-2a** and 1896326 for **S-2b**). These data can be obtained free of charge from the CCDC via www.ccdc.cam.ac.uk/data_request/cif.

2.10. Phase Transition Behavior

The phase transition behaviors of the present bistolanes were observed via polarizing optical microscopy (POM) using an Olympus BX53 microscope (Tokyo, Japan) equipped with a cooling and heating stage (Linkam Scientific Instruments, 10002L; Surrey, UK). The thermodynamic behaviors were determined using a differential scanning calorimeter (DSC, SHIMADZU DSC-60 Plus; Kyoto, Japan) at heating and cooling rates of $5.0\text{ }^\circ\text{C min}^{-1}$ under N_2 atmosphere.

2.11. Photophysical Behavior

UV-vis absorption spectra were recorded using a JASCO V-500 absorption spectrometer (Tokyo, Japan). Steady-state PL spectra were obtained using a JASCO FP-8500 (Tokyo, Japan) for the room-temperature measurements and a Hitachi F-7000 fluorometer (Tokyo, Japan) during heating and cooling. The absolute PL quantum yields were recorded using a calibrated integrating sphere with a Hamamatsu Photonics C11347-01 Absolute PL Quantum Yield Measurement System (Hamamatsu, Japan).

2.12. Computation

All computations were performed via density functional theory (DFT) using the Gaussian 09 (Revision C.01) package [23]. Geometry optimizations were executed using the CAM-B3LYP hybrid functional [24,25] and 6-31+G(d) basis set with the implicit solvation model, the conductor-like polarizable continuum model (CPCM) [26–28], for CH_2Cl_2 . The excitation energies and dipole moments of the optimized structures were calculated using the time-dependent DFT (TD-DFT) method at the same level as in the theory.

3. Results and Discussion

3.1. Molecular Design, Synthesis, and Crystal Structure

Combining a bistolane-based light-emitting core with a flexible unit with a branch structure would yield prominent LELCs showing unique LE and LC properties. For such promising LELCs, we chose a Cl-containing alkoxy chain for the branch structure, because a Cl atom would significantly influence both the LE and LC characteristics owing to the relatively large electronegativity ($\chi_p = 3.16$, as estimated by Pauling [29]) and the fact that its atomic size is approximately 1.5 times larger (van der Waals radius (r_{vdW}) of 175 pm for Cl [30]) than that of H ($\chi_p = 2.20$, $r_{\text{vdW}} = 120$ pm). Therefore, as shown in Figure 2, we designed the molecular structures **2a** and **2b** with a 2-chloroalkoxy-substituents.

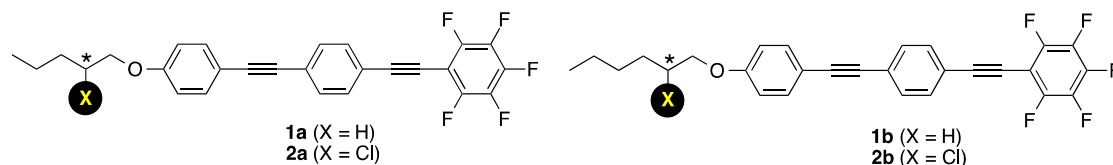


Figure 2. Chemical structures of bistolanes **1a–b** and 2-chloroalkoxy-substituted **2a–b** investigated in this study.

To gain additional insight into the 2-chloroalkoxy-substituted bistolanes **2a** and **2b**, we initially performed DFT calculations using a CAM-B3LYP/6-31+G(d) level of theory. Figure 3 summarizes

the electrostatic potentials and dipole moments of these compounds and provides their highest occupied molecular orbital (HOMO) and lowest unoccupied molecular orbital (LUMO) diagrams. The calculation results for **1a** are also shown for reference.

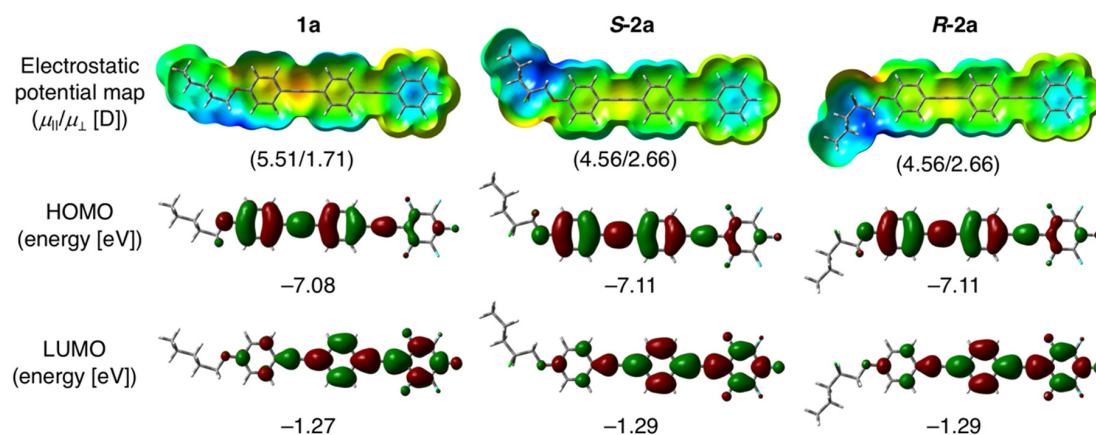


Figure 3. Electrostatic potential map, dipole moment (μ), HOMO diagram, and LUMO diagram for **1a**, **S-2a**, and **R-2a** according to density functional theory (DFT) calculations performing using CAM-B3LYP/6-31+G(d) with the conductor-like polarizable continuum model (CPCM) model (CH_2Cl_2).

By comparing the electrostatic potential maps and the HOMO and LUMO diagrams of **1a** and **S-/R-2a**, it can be seen that incorporating a Cl atom into the flexible unit did not influence the electron-density distribution or the molecular orbital distribution. Incorporating a Cl atom at the 2-position in the flexible unit does not significantly alter the electronic transition process, that is, the absorption and PL properties in solution. On the other hand, the Cl atoms in **S-2a** and **R-2a** enhanced the molecular dipole moment (μ_{\perp}) in the short molecular axis direction due to the electronegative character of the Cl atom compared to an H atom. The change in the dipole moment between **1a** and **S-/R-2a** may induce dramatic alterations in molecular arrangements in condensed phases, which would provide significant changes in the LC and PL properties in condensed phases. The theoretical evaluation clearly demonstrated that the molecular design is reasonable for novel LELCs.

Based on the molecular design, as shown in Scheme 1, we synthesized target pentafluorinated bistolanes **2a** and **2b** with 2-chloropentyloxy or 2-chlorohexyloxy chains, which were obtained in three steps from the corresponding 4-alkoxyphenylacetylene **3a** or **3b**. Among the 2-chloroalkoxy-substituted pentafluorinated bistolanes obtained, **S-2a**, **R-2a**, and **S-2b** furnished single crystals suitable for X-ray crystallographic analysis. The crystal structures of **S-2a** and **R-2a** are shown in Figure 4. The **S-2a** and **R-2a** with 2-chloropentyloxy flexible units were crystallized with triclinic crystalline systems in the $P1$ space group, and each of the unit cells contained two molecules. On the contrary, the (*S*)-2-chlorohexyloxy-substituted analogue, **S-2b**, possessed a monoclinic crystal structure belonging to the $P2_1$ space group and contained four molecules in a unit cell (Figure S1, in the supplementary materials). The absolute configurations at the chiral centers for these compounds were conveniently determined using the Flack parameter ($\chi = -0.06(8)$ for **S-2a**, $0.10(4)$ for **R-2a**, and $0.10(4)$ for **S-2b**) [31].

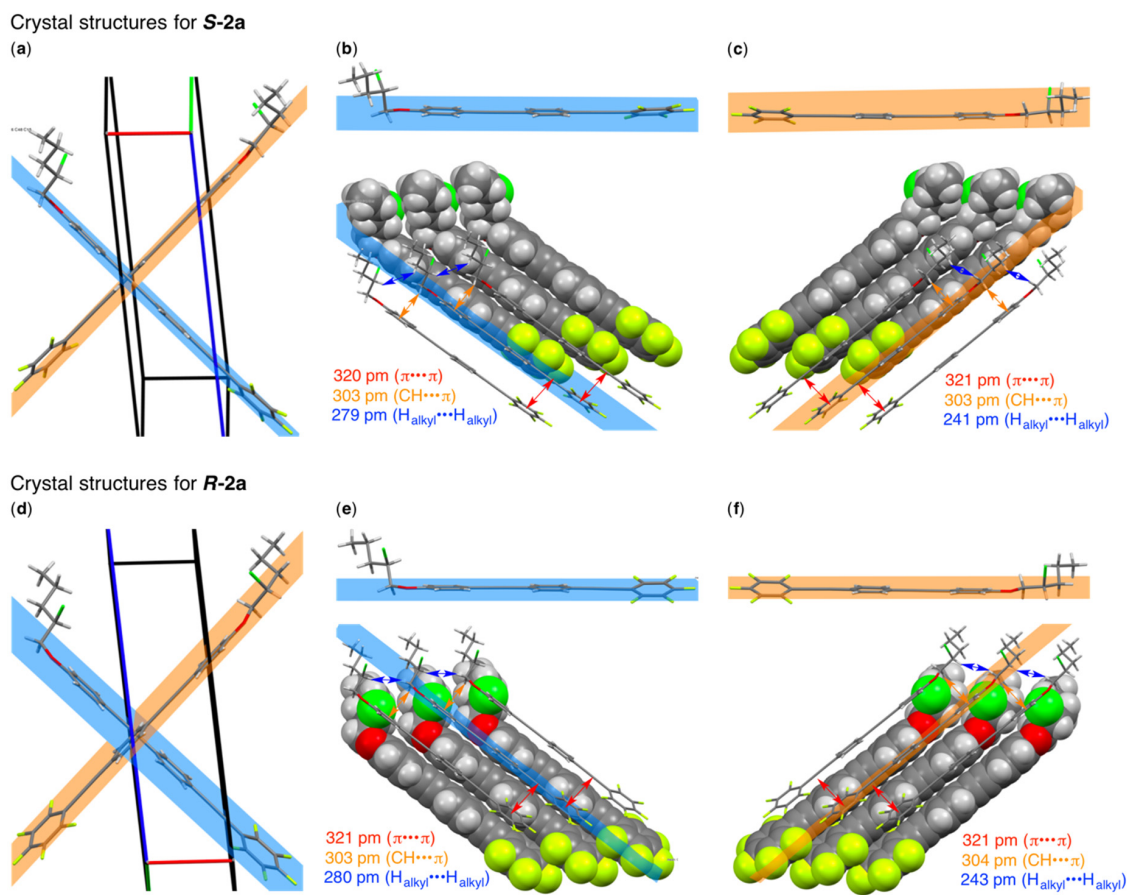


Figure 4. (a) Crystal structures in a unit cell and (b,c) (top) side view and (bottom) packing structures for **S-2a**. (d) Crystal structures in a unit cell and (e,f) (top) side view and (bottom) packing structures for **R-2a**. Arrows: shortest contact for $\pi \cdots \pi$ (red), for $\text{CH} \cdots \pi$ (yellow), and for $\text{H} \cdots \text{H}$ (blue).

As shown in Figure 4a,d, **S-2a** and **R-2a** were each found to consist of two molecules with slightly different structures in a unit cell: one possessed a 2-chloroalkoxy unit at approximately 80° to a blue-colored bistolane structure (Figure 4b), and the other carried the flexible chain at $\sim 5^\circ$ to an orange-colored bistolane core (Figure 4c). As shown in Figure 4b,c (top), three aromatic rings in the bistolane structure formed planar structures, although the three aromatic rings could be in rapid equilibrium between coplanar and twisted conformations through $C_{sp2}-C_{sp}$ single bonds. As shown in Figure 4b (bottom), the packing constructed by blue-colored bistolanes was realized by several intermolecular interactions, such as π/π stacking ($\pi \cdots \pi$: 320 pm on average) and CH/π interaction ($\text{CH} \cdots \pi$: 303 pm on average). In contrast, as shown in Figure 4c (bottom), orange-colored molecules formed packing structures with short contact between not only $\pi \cdots \pi$ and $\text{CH} \cdots \pi$, but also between flexible moieties ($\text{H}_{\text{alkyl}} \cdots \text{H}_{\text{alkyl}}$: 241 pm on average). The shortest atomic distances were almost equal to or shorter than the sums of the van der Waals (vdW) radii (carbon: 170 pm and hydrogen: 120 pm [30]) of the two atoms; consequently, the tight molecular packing in the crystal is strongly attributable to two or three intermolecular interactions, namely π/π , CH/π and vdW. Similarly, as shown in Figure 4e,f, **R-2a** possessed two kinds of molecules in a unit cell and was constructed by intermolecular interactions in the crystal lattice as well.

3.2. Phase Transition Behavior

With the 2-chloroalkoxy-substituted pentafluorinated bistolanes, our attention was directed toward the phase transition behavior, which was measured via POM and using a DSC. The phase

sequence and temperature observed using the DSC are summarized in Table 1, and the POM images in the LC phase are shown in Figure 5.

Table 1. Phase transition behavior of **2a** and **2b** in the second heating and cooling process.

Compound	Phase Sequence and Temperature (Enthalpy, kJ mol ⁻¹) ^{1,2}	
S-2a	Heating	Cr ¹ 60 (−16.6) Cr ² 130 (58.1) N* 148 (0.35) Iso
	Cooling	Iso 148 (−0.44) BP ³ 146 (−) ⁴ N* 112 (−0.84) SmA 97 (−29.2) Cr ¹
R-2a	Heating	Cr ¹ 60 (−29.6) Cr ² 130 (50.9) N* 148 (0.35) Iso
	Cooling	Iso 148 (−0.31) BP ³ 147 (−) ⁴ N* 111 (−0.62) SmA 102 (−29.0) Cr ¹
rac-2a	Heating	Cr ¹ 83 (−12.7) Cr ² 118 (43.1) SmA 126 (−) ³ N 155 (0.33) Iso
	Cooling	Iso 154 (−0.33) N 115 (−0.44) SmA 102 (−25.2) Cr ¹
S-2b	Heating	Cr ¹ 74 (−16.4) Cr ² 130 (59.2) N* 143 (0.38) Iso
	Cooling	Iso 144 (−0.52) BP ³ 142 (−) ⁴ N* 116 (−0.84) SmA 89 (−28.6) Cr ¹
rac-2b	Heating	Cr ¹ 75 (−12.1) Cr ² 110 (−3.2) Cr ³ 130 (43.2) N 142 (0.28) Iso
	Cooling	Iso 143 (−0.38) N 115 (−0.65) SmA 88 (−19.8) Cr ² 85 (−0.24) Cr ¹

¹ Abbreviations: Cr: crystal, SmA: smectic A, N*: chiral nematic, BP: blue phase, and Iso: isotropic phases. ² The temperature was determined by using a differential scanning calorimeter (DSC; 5.0 °C min⁻¹, N₂ atmosphere). ³ The BP phase was determined via polarizing optical microscopy (POM). ⁴ The phase transition enthalpy could not be determined due to the narrow temperature range.

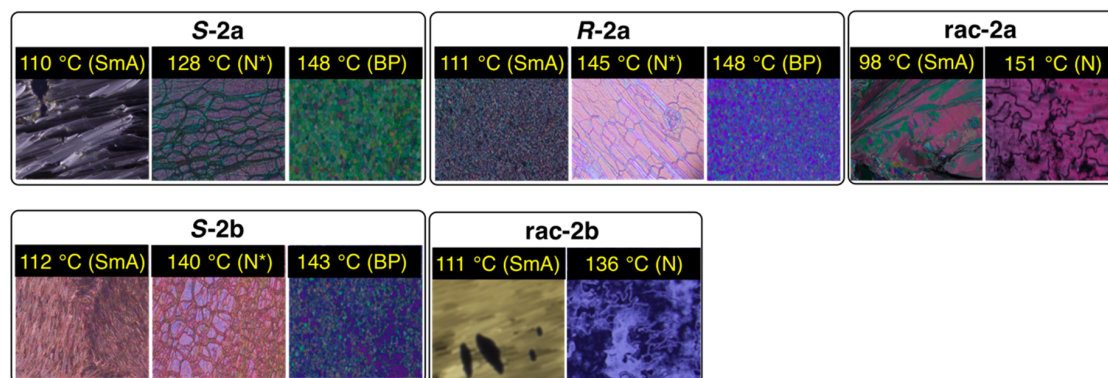


Figure 5. POM images of the LC phases observed in the second cooling process.

All bistolane derivatives with 2-chloroalkoxy flexible units showed LC phases during both heating and cooling. In the DSC measurements, **S-2a** displays a LC phase during the heating process, while two LCs are observed during cooling. The POM results obtained during heating reveal dynamic phase changes from the Cr phase with a nonfluidic bright-viewing field to the LC phase with a fluidic bright-viewing texture at 130 °C and from the LC phase to an isotropic (Iso) liquid phase with a fluidic dark-viewing field at 148 °C. The POM image of the LC phase displays a Grandjean texture, which is one of the characteristics of a chiral nematic (N*) phase. Upon cooling, on the other hand, a platelet texture between 146 °C and 148 °C and a fan-shaped texture between 97 °C and 112 °C, as well as a Grandjean image (N* phase), are observable via POM. The former platelet texture is typical of optical images for a blue phase (BP) [32–36], and the latter is typical for a smectic (Sm) phase. Considering the phase transition enthalpy and the texture change from bright to dark induced by shearing, the Sm phase can be assigned to the smectic A (SmA) phase [14,15]. The phase transition behavior of **R-2a** is almost identical to that of **S-2a**, whereas **rac-2a**, a racemic mixture, showed SmA and nematic (N) phases, not the N* phase, during both heating and cooling cycles, and a somewhat lower melting temperature (T_m) [37] compared to those of the chiral derivatives. In the case of 2-chlorohexyloxy-substituted bistolanes, e.g., **S-2b** and **rac-2b**, a similar phase transition was observed, but the transition temperature, i.e., T_m and the clearing temperature (T_c), in the cooling cycle slightly decreased ($T_m = 88–89$ °C and $T_c = 143–144$ °C) in comparison with those for the **S-2a** ($T_m = 97$ °C and $T_c = 148$ °C) and **rac-2a** ($T_m = 102$ °C and $T_c = 148$ °C) carrying the flexible 2-chloropentyloxy chain. In comparison with the previously reported phase transition behaviors of the linear analogues

1a and **1b** [15], introduction of Cl into the flexible chain did not significantly change T_m , but did cause a dramatic decrease in T_c . In addition, the Cl substitution in a chiral fashion caused a dramatic change in the appearance of the LC phase, resulting in both N^* and BP phases.

3.3. Photophysical Behavior in Solution

Subsequently, we evaluated the absorption and PL behaviors of the 2-chloroalkoxy-substituted **2a** and **2b** in dilute CH_2Cl_2 solutions (approximately $1.0 \times 10^{-5} \text{ mol L}^{-1}$ solution for absorption and $1.0 \times 10^{-6} \text{ mol L}^{-1}$ solution for PL measurement). The absorption and PL spectra obtained are shown in Figure 6, and the photophysical data are presented in Table 2.

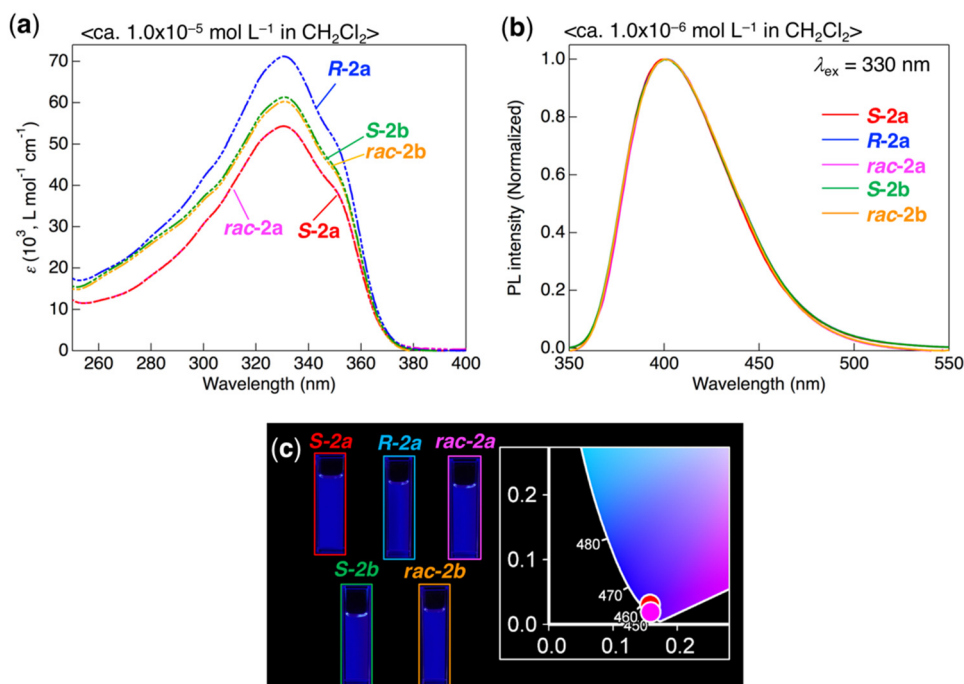


Figure 6. (a) Absorption and (b) PL spectra for **2a** and **2b** in dilute CH_2Cl_2 solution. (c) Photographs of PL under UV irradiation ($\lambda_{\text{ex}} = 365 \text{ nm}$) and the Commission Internationale de l’Eclairage (CIE) chromaticity diagram for the PL.

Table 2. Photophysical (absorption and PL) data of **2a** and **2b** in dilute CH_2Cl_2 solution.

Compound	λ_{abs} (nm) ($\epsilon \times 10^{-3} \text{ L mol}^{-1} \text{ cm}^{-1}$) ¹	λ_{PL} (nm) ²	Φ_{PL} ³
S-2a	330 (54.3), 348 (shoulder, 40.3)	401	0.80
R-2a	330 (71.2), 348 (shoulder, 52.9)	401	0.81
rac-2a	330 (54.3), 348 (shoulder, 40.3)	401	0.80
S-2b	331 (61.3), 349 (shoulder, 45.6)	401	0.88
rac-2b	331 (60.3), 349 (shoulder, 44.7)	401	0.76

¹ Concentration of the solution: ca. $1.0 \times 10^{-5} \text{ mol L}^{-1}$. ² Concentration of the solution: ca. $1.0 \times 10^{-6} \text{ mol L}^{-1}$. Excited at 330 nm. ³ Measured using a calibrated integrating sphere system.

In Figure 6a, all bistolanes with 2-chloroalkoxy chains show an absorption band with a maximum absorption wavelength (λ_{abs}) at 330–331 nm, together with a shoulder at 348–349 nm. To understand the electronic transition in the light-absorption process, TD-DFT calculations were performed for **S-2a**, **R-2a**, and **S-2b** at the same level as the theory with a CPCM model, which revealed that the lowest vertical excitation mainly corresponded to the transition from HOMO to LUMO. As mentioned before, the orbital lobes of the HOMO and LUMO were localized at the electron-rich and electron-deficient aromatic rings, respectively. Consequently, the absorption behavior could be assigned to a π – π^* transition involving intramolecular charge transfer.

When the dilute solution of **S-2a** (concentration: ca. 1.0×10^{-6} mol L⁻¹) was irradiated with 330 nm light, it exhibited intense PL with a maximum wavelength at 401 nm (Figure 6b). As shown in Figure 6c, the PL color was deep blue upon irradiation with 365 nm UV light, where the color coordinates (x, y) were (0.16, 0.03), as defined by the Commission Internationale de l’Eclairage (CIE). The measured PL behavior for the other samples, i.e., **R-2a**, *rac-2a*, **S-2b**, and *rac-2b*, in dilute CH₂Cl₂ solution are presented in Figure 6b. All derivatives show intensive deep-blue PL with $\Phi_{\text{PL}} = 0.76\text{--}0.88$, and their PL spectra are completely identical to the PL spectrum for **S-2a**. This finding clearly indicates that PL in solution does not change depending on the chirality or the flexible-chain length. Comparison with the linear analogue **1a** ($\lambda_{\text{abs}} = 333$ nm, $\lambda_{\text{PL}} = 405$ nm) [15], however, indicates that a slight short-wavelength shift occurred in the presence of Cl atoms in the flexible chain, as in the case of **2a**. It is reasonable that 2-chloroalkoxy flexible units in **2a** decrease the HOMO energy level by inducing the Cl atoms to show high-energy PL as compared with that of the corresponding linear **1a**.

3.4. Photophysical Behavior in the Cr Phase

We next directed our attention toward the PL behavior of the 2-chloroalkoxy-substituted bistolanes **2a** and **2b** in the Cr phase. The obtained PL spectra are presented in Figure 7a, and the photographs and CIE diagram for the PL colors observed are shown in Figure 7b. The photophysical data observed are summarized in Table 3.

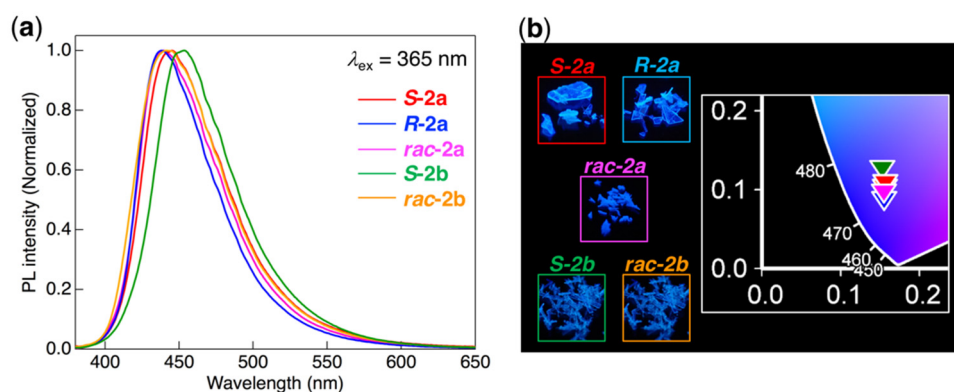


Figure 7. (a) PL spectra for **2a** and **2b** in the crystalline phase. (b) Photographs of PL under UV irradiation ($\lambda_{\text{ex}} = 365$ nm) and CIE chromaticity diagram for the PL colors.

Table 3. Photophysical data of **2a** and **2b** in the crystalline phase.

Compound	λ_{PL} (nm) ¹	Φ_{PL} ²
S-2a	445	0.38
R-2a	438	0.48
<i>rac-2a</i>	440	0.42
S-2b	453	0.54
<i>rac-2b</i>	441	0.55

¹ Excited at 365 nm. ² Measured using a calibrated integrating sphere system.

When **S-2a** in the Cr phase was irradiated with 365 nm light, the **S-2a** exhibited a single PL band with a maximum PL wavelength of 445 nm. Considering the difference between the PL efficiency (Φ_{PL}) of the Cr and solution phases, Φ_{PL} is lower in the Cr phase than in the solution phase due to the nonradiative decay through tight π/π stacking ($\pi \cdots \pi$: 320 pm, Figure 4a) in condensed phases. However, the Φ_{PL} (= 0.38) in the Cr phase was found to be somewhat high, owing to effective molecular motion restriction. The others, i.e., **R-2a**, *rac-2a*, **S-2b**, and *rac-2b*, were also found to emit blue PL in the Cr phase with relatively high PL efficiency ($\Phi_{\text{PL}} = 0.42\text{--}0.55$). From the viewpoint of maximum PL wavelength, in contrast to the PL in dilute solution, the 2-chloroalkoxy-substituted bistolanes **2a** and **2b** showed various PL with the maximum wavelength between 438 nm and 453 nm, and displayed

PL colors from deep blue to light blue (Figure 7a,b). The behavior of *rac-2a* and *rac-2b* was almost identical, resulting in a maximum PL wavelength of ~ 440 nm, whereas the maximum PL wavelength for *R-2a* was slightly shorter (438 nm) and those for *S-2a* and *S-2b* were slightly longer, i.e., 445–453 nm. Considering the reported maximum PL wavelengths for the linear analogues, **1a** and **1b** [15], the slight difference in the alkoxy chain length between C_5H_{11} and C_6H_{13} did not significantly change the PL behavior. Hence, it is reasonable that the present molecules, *S-2a* and *S-2b*, showed similar PL behaviors. Moreover, considering the distinct crystal structures, the PL variations among *rac-2a*, *S-2a*, and *R-2a* can be rationally explained. Thus, as mentioned before, the aggregated structures for *S-2a* and *R-2a* were quite similar, but the interatomic distances, e.g., $\pi \cdots \pi$, $CH \cdots \pi$, and $H_{alkyl} \cdots H_{alkyl}$, observed in the *S-2a* crystals were slightly shorter than those for *R-2a*. Thus, *S-2a* is more tightly packed than *R-2a*, causing a slight red-shift via energy transfer through intermolecular interactions. The crystal volumes of *S-2a* (1117.88 \AA^3) and *R-2a* (1126.45 \AA^3) (Table S1) also indicate that *S-2a* is densely packed, resulting in low-energy PL compared to that of *R-2a*.

3.5. PL Behavior Through Phase Transition upon Heating and Cooling

Regarding novel LELCs, our interest was drawn to the PL behavior in the LC phases. Therefore, the PL with varying measurement temperatures was investigated using a spectrofluorometer attached with a custom-made heating device. The thermoresponsive PL measurements were performed for two selected samples: *R-2a* with λ_{PL} at the shortest wavelength and *S-2b* with λ_{PL} at the longest wavelength in the Cr phase.

Figure 8a shows the PL spectra of *R-2a* during the first cooling cycle from $140 \text{ }^\circ\text{C}$ (N^*) to $40 \text{ }^\circ\text{C}$ (Cr), together with the initial PL spectrum at $40 \text{ }^\circ\text{C}$. Similarly, Figure 8b shows the PL behaviors of *R-2a* during the second heating cycle from $40 \text{ }^\circ\text{C}$ (Cr) to $160 \text{ }^\circ\text{C}$ (Iso) through $140 \text{ }^\circ\text{C}$ (N^*).

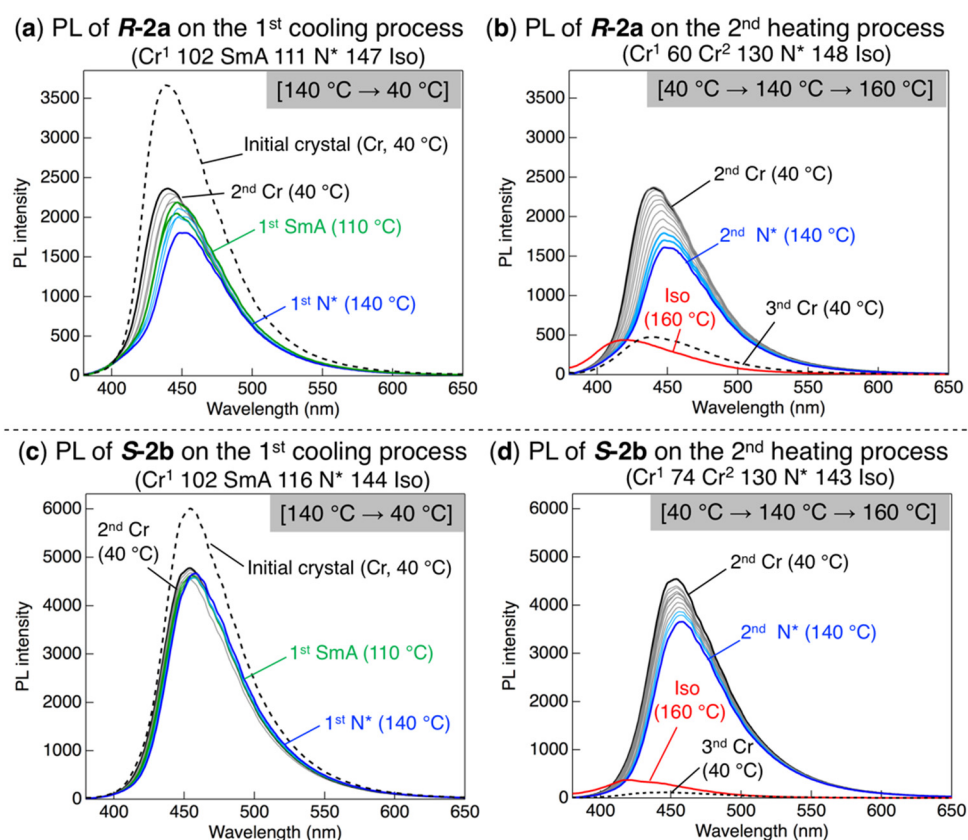


Figure 8. PL behavior of *R-2a* ($\lambda_{ex} = 365$ nm) on the (a) first and (b) second heating and cooling processes. PL behavior of *S-2b* ($\lambda_{ex} = 365$ nm) on the (c) first and (d) second heating and cooling processes. Colors, black: Cr; green: SmA; blue: N^* ; red: Iso phases.

As shown in Figure 8a, λ_{PL} of **R-2a** gradually shifted from 438 nm in the Cr phase (dashed black line) to 453 nm in the N* phase (solid blue line) upon increasing the temperature from 40 °C to 140 °C during the first heating cycle. When the material phase-transitioned from N* to SmA at 111 °C during the first cooling cycle, λ_{PL} decreased by 6 nm, yielding $\lambda_{PL} = 447$ nm. Further cooling resulting in phase transition from SmA to Cr caused λ_{PL} to shift to a shorter wavelength again, this time to 439 nm, which is almost identical to λ_{PL} in the initial Cr phase. The PL intensity gradually decreased with heating, owing to the acceleration of the thermal deactivation through molecular motion, but after the first cooling cycle, 65% of the initial PL intensity was recovered. Subsequently, as shown in Figure 8b, the second heating process inducing the transition from the Cr phase at 40 °C to the N* phase at 140 °C induced λ_{PL} shift to a longer wavelength of 452 nm again. Further heating to the Iso phase at 160 °C caused a significant shift of λ_{PL} to a shorter wavelength of 419 nm with a drastic decrease in the PL intensity. After the second cooling cycle, as shown by the dashed black line in Figure 8b, λ_{PL} returned to 439 nm at the appearance of the third Cr phase, although the PL intensity did not recover at all.

Similarly, Figure 8c shows the PL spectra of **S-2b** acquired during the first heating and cooling cycles. In this case, heating from the Cr phase at 40 °C ($\lambda_{PL} = 453$ nm) to the N* phase at 140 °C caused a slight long-wavelength shift by 5 nm, yielding $\lambda_{PL} = 458$ nm. During the first cooling cycle, the phase transition from N* to SmA at 116 °C induced a slight short-wavelength shift by 2 nm, and further cooling to the Cr phase at 40 °C caused an additional short-wavelength shift, yielding $\lambda_{PL} = 454$ nm. Similar to the PL behavior for **R-2a** mentioned above, the PL intensity reduced upon heating, but the cooling process induced recovery of the PL intensity to 80% of that in the initial Cr phase. As shown in Figure 8d, the phase transition from Cr to N* during the second heating process caused a slight λ_{PL} shift to 458 nm again with a gradual decrease in PL intensity. Further heating through phase transition from the N* phase at 140 °C to the Iso phase at 160 °C caused a drastic decrease in PL intensity due to the complete destruction of the molecular aggregates through thermal-activated molecular motion. It was unfortunate that cooling from the Iso phase at 160 °C to the Cr phase at 40 °C did not lead to the recovery of the PL intensity.

The thermoresponsive PL behaviors of **R-2a** and **S-2b** during the heating and cooling cycles revealed that λ_{PL} was precisely switched depending on the phases observed, namely Cr, SmA, and N*. When the Iso phase was achieved after heating, however, the PL intensity significantly decreased and did not recover at all even after phase transition to Cr.

4. Conclusions

In this study, we designed 2-chloroalkoxy-substituted pentafluorinated bistolanes as novel LELCs and synthesized them from easily accessible 4-(2-chloropentyloxy)- or 4-(2-chlorohexyloxy)phenylacetylene according to established synthetic procedures. The 2-chloroalkoxy-substituted bistolanes displayed the LC phase during both heating and cooling, and in particular, the chiral derivatives showed an N* phase under a polarizing optical microscope. Compared with the racemic and achiral analogues, completely distinct LC phases are likely to result from chirality in the flexible chain. Moreover, very interestingly, the chiral analogues also exhibited a BP only over a narrow temperature range (2–4 °C) according to the POM results, which may be applicable to photonic materials owing to the three-dimensional periodic structure [38–40]. In addition, the pentafluorinated bistolanes with 2-chloroalkoxy flexible chains were found to luminesce not only in a dilute CH₂Cl₂ solution with $\Phi_{PL} = 0.76$ –0.88, but also in the crystalline phase with $\Phi_{PL} = 0.38$ –0.55. It was interesting that λ_{PL} shifted sensitively depending on a change in the stereo configuration as well as the flexible-chain length, which likely originated from a slight difference in the molecular aggregate structures in the crystal. Remarkably, the PL behaviors through phase transition upon heating and cooling clearly revealed that λ_{PL} sensitively shifted through the Cr (\rightleftharpoons SmA) \rightleftharpoons N* phase transition, although the PL intensity gradually decreased after heating and cooling. The PL color changes of the present LELCs are anticipated to be applicable in PL thermometers, although more dynamic color changes are required for practical use.

Supplementary Materials: The following are available online at <http://www.mdpi.com/2073-4352/9/4/195/s1>, Figure S1: Crystal packing structures, Table S1: Crystallographic data, Figure S2: DSC thermograms, Figure S3: Absorption and PL spectra, Figure S4: Excitation and PL spectra, Figure S5: Molecular orbital diagrams for **S-2a** obtained after DFT calculation, Table S2: Cartesian coordinates for **S-2a**, Figure S6: Molecular orbital diagrams for **R-2a** obtained after DFT calculation, Table S3: Cartesian coordinates for **R-2a**, Figure S7: Molecular orbital diagrams for **S-2b** obtained after DFT calculation, Table S4: Cartesian coordinates for **S-2b**.

Author Contributions: Conceptualization, S.Y.; Methodology, S.Y.; Investigation, S.Y., K.M., T.A., T.K. (Toshio Kubota), and T.K. (Tsutomu Konno); Writing—Original Draft Preparation, S.Y. and T.K. (Tsutomu Konno); Writing—Review and Editing, S.Y., K.M., T.A., T.K. (Toshio Kubota), and T.K. (Tsutomu Konno); Visualization, S.Y. and K.M.; Supervision, S.Y.; Project Administration, S.Y.; Funding Acquisition, S.Y. and T.K. (Tsutomu Konno).

Funding: This research was funded by JSPS KAKENHI, a Grant-in-Aid for Scientific Research (C) (Grant No. JP18K05262).

Acknowledgments: We are sincerely grateful to Kensuke Naka and Hiroaki Imoto (Kyoto Institute of Technology) for the absolute PL quantum yield measurements. We also express our gratitude to Osamu Tsutsumi (Ritsumeikan University) for the PL behavior measurements in the LC phases.

Conflicts of Interest: The authors declare no conflict of interest.

References

1. Yang, Y.; Zhao, Q.; Feng, W.; Li, F. Luminescent chemodosimeters for bioimaging. *Chem. Rev.* **2013**, *113*, 192–270. [[CrossRef](#)] [[PubMed](#)]
2. Bünzli, J.-C.G. Lanthanide luminescence for biomedical analyses and imaging. *Chem. Rev.* **2010**, *110*, 2729–2755. [[CrossRef](#)]
3. Zhou, J.; Feng, W.; Sun, Y.; Li, F. Upconversion luminescent materials: Advances and applications. *Chem. Rev.* **2015**, *115*, 395–465. [[CrossRef](#)]
4. Bui, T.T.; Goubard, F.; Ibrahim-Ouali, M.; Gigmes, D.; Dumur, F. Recent advances on organic blue thermally activated delayed fluorescence (TADF) emitters for organic light-emitting diodes (OLEDs). *Beilstein J. Org. Chem.* **2018**, *14*, 282–308. [[CrossRef](#)] [[PubMed](#)]
5. Jhulki, S.; Moorthy, J.N. Small molecular hole-transporting materials (HTMs) in organic light-emitting diodes (OLEDs): Structural diversity and classification. *J. Mater. Chem. C* **2018**, *6*, 8280–8325. [[CrossRef](#)]
6. Hemmer, E.; Acosta-Mora, P.; Méndez-Ramos, J.; Fischer, S. Optical nanoprobe for biomedical applications: Shining a light on upconverting and near-infrared emitting nanoparticles for imaging, thermal sensing, and photodynamic therapy. *J. Mater. Chem. B* **2017**, *5*, 4365–4392. [[CrossRef](#)]
7. Hou, J.-T.; Ren, W.X.; Li, K.; Seo, J.; Sharma, A.; Yu, X.-Q.; Kim, J.S. Fluorescent bioimaging of pH: From design to applications. *Chem. Soc. Rev.* **2017**, *46*, 2076–2090. [[CrossRef](#)]
8. Turro, N.J.; Ramamurthy, V.; Scaiano, J.C. Photophysical radiationless transitions. In *Principles of Molecular Photochemistry: An Introduction*; Turro, N.J., Ramamurthy, V., Scaiano, J., Eds.; University Science Books: Sausalito, California, 2009; pp. 265–318. ISBN 978-1891389573.
9. Grimsdale, A.C.; Chan, K.L.; Martin, R.E.; Jokisz, P.G.; Holmes, A.B. Synthesis of light-emitting conjugated polymers for applications in electroluminescent devices. *Chem. Rev.* **2009**, *109*, 897–1091. [[CrossRef](#)]
10. Leung, N.L.C.; Xie, N.; Yuan, W.; Liu, Y.; Wu, Q.; Peng, Q.; Miao, Q.; Lam, J.W.Y.; Tang, B.Z. Restriction of intramolecular motions: The general mechanism behind aggregation-induced emission. *Chem. Eur. J.* **2014**, *20*, 15349–15353. [[CrossRef](#)] [[PubMed](#)]
11. Shen, P.; Zhuang, Z.; Zhao, Z.; Tang, B.Z. AIEgens based on main group heterocycles. *J. Mater. Chem. C* **2018**, *6*, 11835–11852. [[CrossRef](#)]
12. He, Z.; Ke, C.; Tang, B.Z. Journey of aggregation-induced emission research. *ACS Omega* **2018**, *3*, 3267–3277. [[CrossRef](#)]
13. Yamada, S.; Mitsuda, A.; Miyano, K.; Tanaka, T.; Morita, M.; Agou, T.; Kubota, T.; Konno, T. Development of novel solid-state light-emitting materials based on pentafluorinated tolane fluorophores. *ACS Omega* **2018**, *3*, 9105–9113. [[CrossRef](#)]
14. Yamada, S.; Morita, M.; Agou, T.; Kubota, T.; Ichikawa, T.; Konno, T. Thermoresponsive luminescence properties of polyfluorinated bistolane-type light-emitting liquid crystals. *Org. Biomol. Chem.* **2018**, *16*, 5609–5617. [[CrossRef](#)] [[PubMed](#)]

15. Yamada, S.; Miyano, K.; Konno, T.; Agou, T.; Kubota, T.; Hosokai, T. Fluorine-containing bistolanes as light-emitting liquid crystalline molecules. *Org. Biomol. Chem.* **2017**, *15*, 5949–5958. [[CrossRef](#)]
16. Yamada, S.; Morita, M.; Konno, T. Multi-color photoluminescence induced by electron-density distribution of fluorinated bistolane derivatives. *J. Fluorine Chem.* **2017**, *202*, 54–64. [[CrossRef](#)]
17. Liu, T.; Zhu, D.; Zhang, M.; Cui, M.; Li, Q.; Fan, Y.; Wang, H.; Zeng, Z. N-fused ring strategy toward orange/yellow light-emitting liquid crystalline molecules. *Dyes Pig.* **2018**, *159*, 115–120. [[CrossRef](#)]
18. Yamada, S.; Rokusha, Y.; Kawano, R.; Fujisawa, K.; Tsutsumi, O. Mesogenic gold complexes showing aggregation-induced enhancement of phosphorescence in both crystalline and liquid-crystalline phases. *Faraday Discuss.* **2017**, *196*, 269–283. [[CrossRef](#)] [[PubMed](#)]
19. Hu, G.; Billa, M.R.; Kitney, S.P.; Kelly, S.M. Symmetrical carbazole-fluorene-carbazole nematic liquid crystals as electroluminescent organic semiconductors. *Liq. Cryst.* **2017**, *45*, 965–979. [[CrossRef](#)]
20. Achalkumar, A.S.; Veerabhadraswamy, B.N.; Hiremath, U.S.; Rao, D.S.S.; Prasad, S.K.; Yelamaggad, C.V. Photoluminescent discotic liquid crystals derived from tris(*N*-salicylideneaniline) and stilbene conjugates: Structure-property correlations. *Dyes Pig.* **2016**, *132*, 291–305. [[CrossRef](#)]
21. Yamada, S.; Tanaka, T.; Ichikawa, T.; Konno, T. Novel V- and Y-shaped light-emitting liquid crystals with pentafluorinated bistolane-based luminophores. *ACS Omega* **2019**, *4*, 3922–3932. [[CrossRef](#)]
22. Sheldrick, G.M. Crystal structure refinement with SHELXL. *Acta Cryst.* **2015**, *C71*, 3–8. [[CrossRef](#)]
23. Frish, M.J.; Trucks, G.W.; Schlegel, H.B.; Scuseria, G.E.; Robb, M.A.; Cheeseman, J.R.; Scalmani, G.; Barone, V.; Mennucci, B.; Peterson, G.A.; et al. *Gaussian 09*; Revision C.01; Gaussian, Inc.: Wallingford, CT, USA, 2013.
24. Yanai, T.; Tew, D.P.; Handy, N.C. A new hybrid exchange-correlation functional using the Coulomb-attenuating method (CAM-B3LYP). *Chem. Phys. Lett.* **2004**, *393*, 51–57. [[CrossRef](#)]
25. Okuno, K.; Shigeta, Y.; Kishi, R.; Nakano, M. Non-empirical tuning of CAM-B3LYP functional in time-dependent density functional theory for excitation energies of diarylethene derivatives. *Chem. Phys. Lett.* **2013**, *585*, 201–206. [[CrossRef](#)]
26. Andzelm, J.; Kölmel, C.; Klamt, A. Incorporation of solvent effects into density functional calculations of molecular energies and geometries. *J. Chem. Phys.* **1995**, *103*, 9312–9320. [[CrossRef](#)]
27. Barone, V.; Cossi, M. Quantum Calculation of molecular energies and energy gradients in solution by a conductor solvent model. *J. Phys. Chem. A* **1998**, *102*, 1995–2001. [[CrossRef](#)]
28. Cossi, M.; Rega, N.; Scalmani, G.; Barone, V. Energies, structures, and electronic properties of molecules in solution with the C-PCM solvation model. *J. Comput. Chem.* **2003**, *24*, 669–681. [[CrossRef](#)] [[PubMed](#)]
29. Murphy, L.R.; Meek, T.L.; Allred, A.L.; Allen, L.C. Evaluation and test of Pauling’s electronegativity scale. *J. Phys. Chem. A* **2000**, *104*, 5867–5871. [[CrossRef](#)]
30. Bondi, A. van der Waals volumes and radii. *J. Phys. Chem.* **1964**, *68*, 441–451. [[CrossRef](#)]
31. Flack, H.D.; Bernardinelli, G. Reporting and evaluating absolute-structure and absolute-configuration determinations. *J. Appl. Cryst.* **2000**, *33*, 1143–1148. [[CrossRef](#)]
32. Coates, D.; Gray, G.W. Optical studies of the amorphous liquid-cholesteric liquid crystal transition: The “blue phase”. *Phys. Lett. A* **1973**, *45*, 115–116. [[CrossRef](#)]
33. Meiboom, S.; Sethna, J.P.; Anderson, P.W.; Brinkman, W.F. Theory of the blue phase of cholesteric liquid crystals. *Phys. Rev. Lett.* **1981**, *46*, 1216–1219. [[CrossRef](#)]
34. Kikuchi, H.; Yokota, M.; Hisakado, Y.; Yang, H.; Kajiyama, T. Polymer-stabilized liquid crystal blue phases. *Nat. Mater.* **2002**, *1*, 64–68. [[CrossRef](#)] [[PubMed](#)]
35. Yoshizawa, A.; Sato, M.; Rokunohe, J. A blue phase observed for a novel chiral compound possessing molecular biaxiality. *J. Mater. Chem.* **2005**, *15*, 3285–3290. [[CrossRef](#)]
36. Coles, H.J.; Pivnenko, M.N. Liquid crystal ‘blue phases’ with a wide temperature range. *Nature* **2005**, *436*, 997–1000. [[CrossRef](#)] [[PubMed](#)]
37. Tamura, R.; Takahashi, H.; Ushio, T. New enantiomeric resolution phenomenon of racemic crystals: Preferential enrichment. *J. Synth. Org. Chem. Jpn.* **1998**, *56*, 22–33. [[CrossRef](#)]
38. Cao, W.; Munoz, A.; Palfy-Muhoray, P.; Taheri, B. Lasing in a three-dimensional photonic crystal of the liquid crystal blue phase II. *Nat. Mater.* **2002**, *1*, 111–113. [[CrossRef](#)] [[PubMed](#)]

39. Yokoyama, S.; Mashiko, S.; Kikuchi, H.; Uchida, K.; Nagamura, T. Laser emission from a polymer-stabilized liquid-crystalline blue phase. *Adv. Mater.* **2006**, *18*, 48–51. [[CrossRef](#)]
40. Yoshizawa, A. Material design for blue phase liquid crystals and their electro-optical effects. *RSC Adv.* **2013**, *3*, 25475–25497. [[CrossRef](#)]



© 2019 by the authors. Licensee MDPI, Basel, Switzerland. This article is an open access article distributed under the terms and conditions of the Creative Commons Attribution (CC BY) license (<http://creativecommons.org/licenses/by/4.0/>).